

## A VIRTUAL ANALOG MODEL OF THE EDP WASP VCF

Lasse Köper, Martin Holters

Department of Signal Processing and Communications  
Helmut Schmidt University  
Hamburg, Germany  
lasse.koeper@hsu-hh.de  
martin.holters@hsu-hh.de

Fabián Esqueda, Julian D. Parker

Native Instruments GmbH  
Berlin, Germany  
firstname.lastname@native-instruments.de

### ABSTRACT

In this paper we present a virtual analog model of the voltage-controlled filter used in the EDP Wasp synthesizer. This circuit is an interesting case study for virtual analog modeling due to its characteristic nonlinear and highly dynamic behavior which can be attributed to its unusual design. The Wasp filter consists of a state variable filter topology implemented using operational transconductance amplifiers (OTAs) as the cutoff-control elements and CMOS inverters in lieu of operational amplifiers, all powered by a unipolar power supply. In order to accurately model the behavior of the circuit we propose extended models for its nonlinear components, focusing particularly on the OTAs. The proposed component models are used inside a white-box circuit modeling framework to create a digital simulation of the filter which retains the interesting characteristics of the original device.

### 1. INTRODUCTION

The Wasp is a two-oscillator monophonic synthesizer released in 1978, and designed by synthesist Adrian Wagner (1952–2018) and electronics designer Chris Huggett (1949–2020), founders of the British company Electronic Dream Plant (EDP). From the outset, Wagner and Huggett’s plan was to design an instrument that could compete sound-wise with the popular Korg, Roland and Moog synthesizers of the era, but would only cost a fraction of the price. To achieve this, they came up with a number of cost-saving compromises, such as the use of a cheap black ABS plastic enclosure and a flat two-octave touch-sensitive interface instead of a mechanical keyboard. At the time of its release the Wasp listed for only £199, less than half the price of similarly featured synthesizers [1, 2].

In addition to the cosmetic and interface compromises, the Wasp also featured several cost-saving measures underneath its cheap plastic enclosure. For example, it featured digital oscillators which were implemented using transistor-transistor logic (TTL) circuits, as opposed to the more expensive microprocessor option. For the filter, Huggett opted for a second-order (12 dB/octave) multimode *state variable filter* (SVF) design implemented using CMOS inverters as a low-cost alternative to operational amplifiers. While not strictly an original idea [3], the use of CMOS inverters is relatively uncommon in synthesizer filter designs. An additional peculiarity of the original Wasp synthesizer is the fact that it operated on a single +5 V unipolar power supply. This design specification, together with its unusual filter design, played a major role in giving

the Wasp filter its characteristic voice, which is usually described as “dirty” sounding [4]<sup>1</sup>. Between 1980–1981 Huggett released the Gnat synthesizer, a single-oscillator version of the Wasp that also featured a CMOS inverter-based VCF [1, 5]. Following the end of EDP, Huggett continued to work as a synthesizer designer, releasing the OSCar (under the company name Oxford Synthesizer Company) and collaborating with Novation on the design of the Bass Station and Bass Station II synthesizers [6].

In 2013 German manufacturer Doepfer released a version of the Wasp filter for the popular Eurorack modular format [4], generating renewed interest in the sound of Chris Huggett’s classic design. More recently, in 2019, German audio company Behringer launched a modernized replica of the Wasp synthesizer<sup>2</sup>. Given the popularity of the Wasp and of its peculiar filter, it is desirable to study its behavior and to attempt to create an accurate virtual analog (VA) model that can be used in software-based music production. Previous research in the field of VA modeling has studied the behavior of different synthesizer filters, such as the classic Moog ladder [7], the EMS VCS3 [8], and the Korg MS-20 and MS-50 synthesizers [9, 10].

In this work we study the behavior of the Wasp filter and propose two extended nonlinear models of the operational transconductance amplifiers (OTAs) and CMOS inverters used in its design. These models allow us to accurately emulate the characteristic nonlinear behavior of the original circuit and provide an insight into what makes the design of the Wasp filter different from that of other synthesizer circuits. This work is organized as follows. Section 2 presents a general overview of the circuit and its fundamental design blocks, together with a linear analysis. Section 3 discusses the nonlinear elements in the circuit and the approach followed to accurately emulate their behavior within the context of the Wasp filter. Finally, Section 4 and 5 provide results of the proposed circuit model and concluding remarks, respectively.

### 2. CIRCUIT DESCRIPTION

In this section, we provide a top-level overview of the Wasp filter and its building blocks, together with a small-signal linear analysis of the circuit.

#### 2.1. The State Variable Filter

The SVF is a common filter design for synthesizer circuits due to its versatility, as it is capable of generating lowpass, highpass and bandpass outputs simultaneously [11]. Figure 1(a) shows a

Copyright: © 2022 Lasse Köper et al. This is an open-access article distributed under the terms of the Creative Commons Attribution 4.0 International License, which permits unrestricted use, distribution, adaptation, and reproduction in any medium, provided the original author and source are credited.

<sup>1</sup>Sound examples that showcase this characteristic behavior can be found in [4].

<sup>2</sup><https://www.behringer.com/product.html?modelCode=P0DN6>

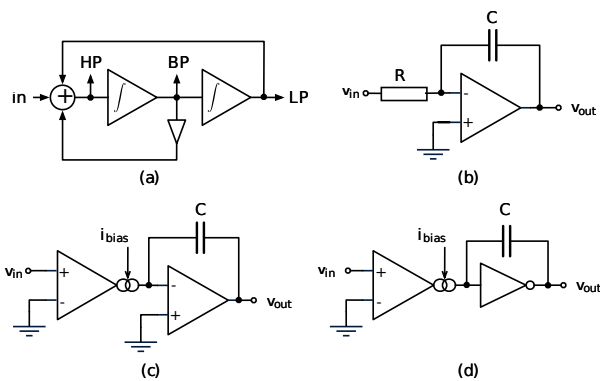


Figure 1: (a) Block diagram representation of a second-order SVF with highpass (HP), bandpass (BP) and lowpass (LP) outputs, and circuit schematics for (b) an RC static integrator, (c) and OTA-based integrator and (d) a CMOS inverter-based integrator circuit.

block diagram representation of a second-order SVF. As shown in this figure, a SVF is comprised of two integrating stages and a summing element setup in a negative feedback configuration. The gain element in the intermediate feedback path is used to control the resonance of the filter which, in some cases, can be configured to enable self-oscillation.

In order to highlight how the design of the Wasp filter circuit differs from that of a traditional SVF we consider the case of the ideal RC integrator circuit shown in Fig. 1(b)<sup>3</sup>, which has the input-output relationship

$$v_{out} = - \int \frac{v_{in}}{RC} dt. \quad (1)$$

This circuit inverts the polarity of the input signal, scales it by the RC *time constant* and computes its integral w.r.t. time [12]. Due to the inverting nature of this circuit, it can be used together with a standard summing amplifier to implement an SVF. The *crossover frequency* of the ideal integrator, i.e. the frequency at which the gain is 0 dB, is given by the time constant as  $f_b = 1/(2\pi RC)$ .

In a musical context, where parametric behavior is desired, it is typical to replace the resistive element in the integrator with a voltage-controlled component such as an OTA, as shown in Fig. 1(c). In the linear regime, under the assumption of infinite input impedance, an OTA obeys the relationship

$$i_{OTA} = i_{bias} \left( \frac{v_+ - v_-}{2V_{TH}} \right), \quad (2)$$

where  $i_{OTA}$  is the current generated by the OTA,  $v_+$  and  $v_-$  are the input voltages at the non-inverting and inverting terminals, respectively,  $V_{TH} \approx 25$  mV is the thermal voltage and  $i_{bias}$  is the *amplifier bias current* which controls the transconductance of the amplifier [13, 14]. The crossover frequency of this ideal OTA-controlled integrator can be adjusted via  $i_{bias}$  and is defined as  $f_b = i_{bias}/(4\pi V_{TH} C)$ .

As mentioned before, one of the most striking aspects of the design of the Wasp filter is its use of CMOS inverters instead of

<sup>3</sup>In practice, this circuit suffers from a number of problems (e.g. at low frequencies the op-amp goes into open loop configuration), so a modified version is more commonly used.

Element	Value
$R_1, R_2, R_3, R_4, R_7, R_8, R_{11}, R_{12}$	27 k $\Omega$
$R_5, R_9$	47 k $\Omega$
$R_6, R_{10}, R_{14}$	1 k $\Omega$
$R_{13}$	1 M $\Omega$
$R_{15}$	100 k $\Omega$
$C_1, C_7$	0.22 $\mu$ F
$C_2$	100 pF
$C_3, C_4$	330 pF
$C_5, C_6$	10 $\mu$ F
$R_{level}$	50 k $\Omega$ linear
$R_{res}$	50 k $\Omega$ linear
$D_1, D_2$	1N4148
$IC_1, IC_3, IC_5$	CD4069
$IC_2, IC_4$	CA3080

Table 1: Wasp Filter Component Values

op-amps<sup>4</sup>. Figure 1(d) shows the circuit schematic for a CMOS inverter-based integrator circuit [3]. Assuming that the inverter has infinite input impedance and infinite (inverting) gain, we can treat the input pin as being tied to the reference voltage. Therefore, the CMOS inverter acts like an ideal op-amp with the non-inverting input tied to ground. In this idealized regime, the behavior of this integrator is identical to that of Fig. 1(c) and hence its crossover frequency is given by the same expression.

Figure 2 shows the complete schematic of the Wasp filter. Component values can be found in Table 1. This schematic is based on the Doepfer version of the circuit which, for the most part, follows Huggett's original design. The only major differences between this circuit and its original counterpart are the value of resistor  $R_{13}$ , which in the EDP version is listed as 100k $\Omega$  and the fact that all ICs are powered using a unipolar +12 V power supply instead of +5 V as in the original. These two modifications accentuate the characteristic erratic and "dirty" sounding behavior of the filter [15], and as such, we have decided to include them as part of this study.

Overall, the Wasp filter follows the general structure of the SVF filter shown in Fig. 1(a), with the CMOS inverter labeled IC1 operating as the summing stage, and ICs 3 and 5 acting as the integrator amplifiers. The ICs labeled 2 and 4 are the OTAs used to control the overall cutoff frequency of the system (via bias currents 1 and 2). The global feedback loop can be seen between the output of the second integrator ( $IC_5$ ) and resistor  $R_2$ , while the intermediate feedback path connects the output of the first integrator ( $IC_2$ ) with the input of the summing stage via a parametric resistive network that controls the resonance of the filter (i.e. acting as the gain element in Fig. 1(a)).

## 2.2. Small-signal Analysis

Having discussed the general design and structure of the Wasp filter, we move on to studying its linear small-signal behavior. Assuming the two diodes in the feedback path are unbiased (i.e. their currents are negligibly small), and carrying on with the assumptions made in the previous section regarding the behavior of the OTAs and the CMOS inverters, we begin our analysis by examining the two integrator stages. Ignoring DC bias,  $R_7$  connects to GND instead

<sup>4</sup>Specifically, the Wasp utilized the CD4069 which packages six CMOS inverter circuits in a single chip.

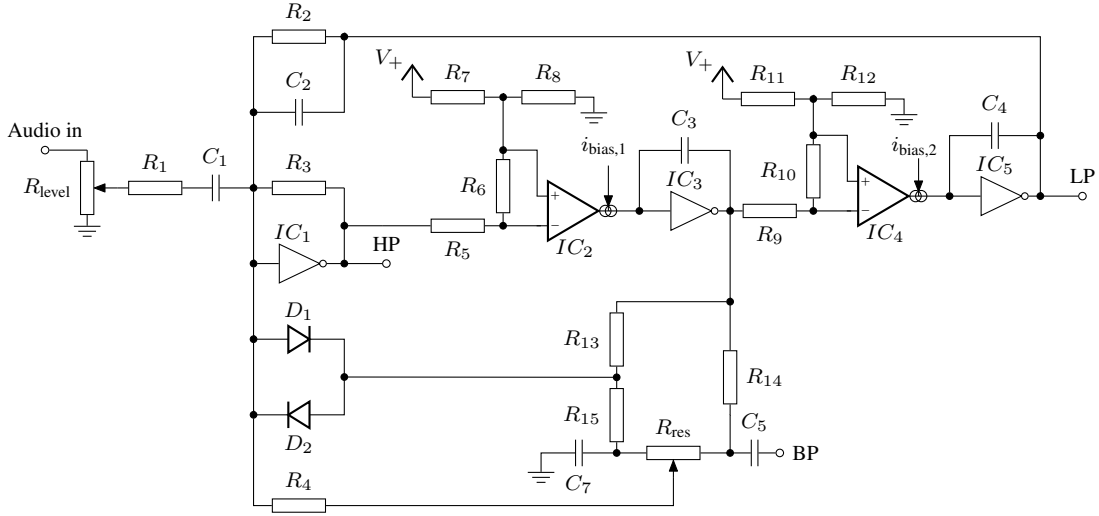


Figure 2: Signal Path Schematic of the Wasp Filter

of +12V, so that  $R_7$  and  $R_8$  are effectively in parallel. Thus, these two resistors together with  $R_6$  and  $R_5$  form a voltage divider which translates the voltage from the preceding CMOS inverter's output to the OTA input voltage by multiplying it with

$$V_+ - V_- = -\frac{R_6}{\frac{R_7 R_8}{R_7 + R_8} + R_5 + R_6} v_{IC1} \approx -16.26 \times 10^{-3} v_{IC1}. \quad (3)$$

To maintain a current-free CMOS input, all of the OTA output current  $i_{IC2}$  charges  $C_3$ , with the output voltage of the CMOS being driven appropriately, i.e.

$$v_{IC3} = -\int \frac{i_{IC2}}{C_3} dt \quad (4)$$

or, considering the Laplace transform instead,

$$v_{IC3} = -\frac{i_{IC2}}{sC_3}. \quad (5)$$

Combined, this leads to

$$v_{IC3} = \frac{1}{sC_3} \cdot i_{bias} \cdot \frac{1}{2V_T} \cdot \frac{R_6}{\frac{R_8 R_7}{R_8 + R_7} + R_6 + R_5} v_{IC1} = \omega_c \cdot \frac{v_{IC1}}{s} \quad (6)$$

with

$$\omega_c = \frac{i_{bias}}{2C_3 V_T} \cdot \frac{R_6}{\frac{R_8 R_7}{R_8 + R_7} + R_6 + R_5} \approx 9.855 \times 10^8 \cdot i_{bias} \quad (7)$$

and likewise

$$v_{IC5} = \omega_c \cdot \frac{v_{IC3}}{s} \quad (8)$$

as the subcircuits around the two inverter/OTA combinations are equivalent including identical component values.

The first CMOS inverter acts as an inverting amplifier, summing its inputs weighted with the ratio of the feedback resistor  $R_3$  and the respective input impedances, i.e.

$$v_{IC1} = -R_3 \cdot \left( \frac{1}{Z_{in}} v_{in} + \frac{1}{Z_1} v_{IC3} + \frac{1}{Z_2} v_{IC5} \right) \quad (9)$$

where

$$Z_{in} = \frac{R_1 + \frac{1}{sC_1} + (1 - \nu)\nu R_{level}}{\nu} \quad Z_2 = \frac{R_2}{1 + sR_2 C_2}, \quad (10)$$

with  $\nu \in [0, 1]$  denoting the setting of the level potentiometer and  $Z_1$  is determined by the more complicated feedback network to be discussed momentarily. For the moment, let  $H_{(\cdot)} = \frac{R_3}{Z_{(\cdot)}}$ , so that

$$v_{IC1} = -(H_{in} v_{in} + H_1 v_{IC3} + H_2 v_{IC5}). \quad (11)$$

We can combine with (6) and (8) and solve to obtain

$$v_{IC1} = H_{HP}(s) H_{in}(s) v_{in} \quad (12)$$

$$v_{IC3} = H_{BP}(s) H_{in}(s) v_{in} \quad (13)$$

$$v_{IC5} = H_{LP}(s) H_{in}(s) v_{in} \quad (14)$$

with

$$H_{HP}(s) = -\frac{s^2}{s^2 + H_1(s)\omega_c s + H_2(s)\omega_c^2} \quad (15)$$

$$H_{BP}(s) = -\frac{\omega_c s}{s^2 + H_1(s)\omega_c s + H_2(s)\omega_c^2} \quad (16)$$

$$H_{LP}(s) = -\frac{\omega_c^2}{s^2 + H_1(s)\omega_c s + H_2(s)\omega_c^2} \quad (17)$$

where

$$H_{in}(s) = \frac{s\nu R_3 C_1}{1 + s(R_1 + (1 - \nu)\nu R_{level})C_1} \quad (18)$$

is a first-order high-pass (AC-coupling) with a cutoff frequency of  $\frac{1}{2\pi(R_1 + (1 - \nu)\nu R_{level})C_1}$ , varying between 18.3 Hz and 26.8 Hz depending on  $\nu$ , and a passband gain of  $\frac{\nu R_3}{R_1 + (1 - \nu)\nu R_{level}}$ , reaching the maximum  $\frac{R_3}{R_1} = 1$  for  $\nu = 1$ , assuming a low-impedance source. For non-negligible source impedance, both cutoff frequency and gain decrease.

In the following, we shall further analyze the denominator

$$D(s) = s^2 + H_1(s)\omega_c s + H_2(s)\omega_c^2. \quad (19)$$

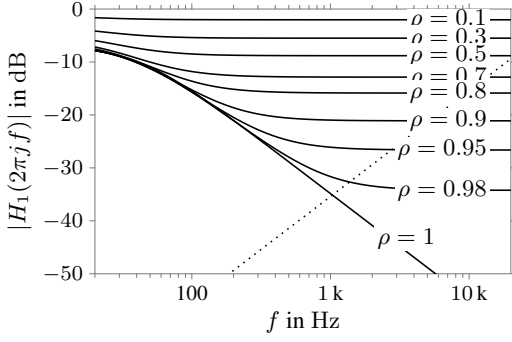


Figure 3: Magnitude transfer functions of  $H_1$  (solid) and  $2\pi R_2 C_2 f$  (dotted)

We first observe that  $H_2(s) = \frac{R_3(1+sR_2C_2)}{R_2} = 1 + sR_2C_2$  as  $\frac{R_3}{R_2} = 1$ . Substituting in (19) leads to

$$D(s) = s^2 + (H_1(s) + R_2C_2\omega_c)\omega_c s + \omega_c^2. \quad (20)$$

Now for  $H_1$ , we apply  $\Delta$ -to- $Y$  transformation to the triangle formed by the two parts of the resonance potentiometer, denoted by  $\rho \cdot R_{res}$  and  $(1 - \rho) \cdot R_{res}$ , where  $\rho \in [0, 1]$  is the setting of the resonance control,  $R_{13} + R_{15}$ , and  $R_{14}$ . By adding  $C_7$  and  $R_4$  to the respective legs of the resulting star, we obtain

$$Z_a = R_a = \frac{(\rho R_{res} + R_{14})(R_{13} + R_{15})}{R_{res} + R_{13} + R_{14} + R_{15}} \quad (21)$$

$$Z_b = R_b + \frac{1}{sC_7} = \frac{(1 - \rho)R_{res}(R_{13} + R_{15})}{R_{res} + R_{13} + R_{14} + R_{15}} + \frac{1}{sC_7} \quad (22)$$

$$Z_c = R_c + R_4 = \frac{(\rho R_{res} + R_{14}) \cdot (1 - \rho)R_{res}}{R_{res} + R_{13} + R_{14} + R_{15}} + R_4. \quad (23)$$

Using  $Y$ -to- $\Delta$  transformation to transform this extended star back to a triangle gives

$$Z_1 = \frac{Z_b Z_c + Z_a Z_b + Z_a Z_c}{Z_b}. \quad (24)$$

Note: no current flows between GND and the input of IC1 (assumed virtually grounded), and the load to IC3 is ignored, so the other triangle impedances are not needed. It follows that

$$H_1(s) = \frac{R_3}{Z_1} = \frac{b_1 s + b_0}{a_1 s + a_0}, \quad (25)$$

with

$$b_1 = R_3(1 - \rho)R_{res}(R_{13} + R_{15})C_7 \quad (26)$$

$$b_0 = R_3(R_{res} + R_{13} + R_{14} + R_{15}) \quad (27)$$

$$a_1 = (R'_{res}(\rho) \cdot (1 - \rho)R_{res} + (R_{res} + R_{14})R_4)(R_{13} + R_{15})C_7 \quad (28)$$

$$a_0 = (R'_{res}(\rho) + R_4) \cdot (R_{res} + R_{13} + R_{14} + R_{15}) - (R'_{res}(\rho))^2, \quad (29)$$

where  $R'_{res}(\rho) = \rho R_{res} + R_{14}$ . The resulting magnitude transfer functions of  $H_1$  for different values of  $\rho$  are shown in Fig. 3. The dotted line furthermore shows  $R_2 C_2 \omega_c$  in dependence of the cutoff frequency  $\omega_c$ .

It can be verified that  $|H_1(j\omega) + R_2 C_2 \omega_c| \leq 1$ . Hence, for low frequencies  $\omega \ll \omega_c$ ,  $D(s)$  is dominated by the  $\omega_c^2$  term while for high frequencies  $\omega \gg \omega_c$  it is dominated by the  $s^2$  term. Only for frequencies close to  $\omega_c$ , the term  $(H_1(s) + R_2 C_2 \omega_c)\omega_c s$  is of significance. In fact, for  $\omega = \omega_c$ , we immediately find

$$\begin{aligned} |H_{HP}(j\omega_c)| &= |H_{LP}(j\omega_c)| = |H_{BP}(j\omega_c)| \\ &= \left| \frac{1}{H_1(j\omega_c) + R_2 C_2 \omega_c} \right|. \end{aligned} \quad (30)$$

In general, if  $H_1(j\omega) + R_2 C_2 \omega_c$  is approximately constant around  $\omega_c$ , the overall filter behavior is well approximated by a second-order state-variable filter with the denominator

$$D(s) = s^2 + \frac{\omega_c}{Q}s + \omega_c^2 \quad (31)$$

with  $Q$ -factor

$$Q = \frac{1}{\Re(H_1(j\omega_c)) + R_2 C_2 \omega_c}. \quad (32)$$

This approximation holds if  $H_1(j\omega)$  is nearly constant around  $\omega_c$ , i.e. for low resonance settings  $\rho$  or high cutoff frequencies  $\omega_c$ , or if  $|H_1(j\omega)| \ll R_2 C_2 \omega_c$ , i.e. for high resonance settings and high cutoff frequencies. Conversely, the approximation does not hold for high resonance settings combined with a low  $\omega_c$ .

The magnitude transfer function of the lowpass part  $H_{LP}(j\omega)$  is shown in Fig. 4 for various cutoff frequency and resonance setting, using the exact denominator given by (20) in black and the approximation according to (31) and (32) in gray. As can be verified, for high cutoff frequencies or low resonance settings, the approximation is valid. For the combination of low cutoff frequency and high resonance, the resonance peak of the exact model is even more pronounced and slightly shifted to higher frequencies compared to the second-order SVF approximation.

### 3. OTA AND CMOS INVERTER MODEL

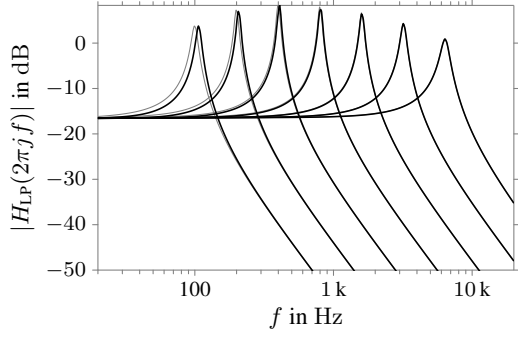
Even though a linear and simplified model is helpful for a general understanding of the Wasp filter's behavior, most of its interesting and beloved sounds can only be explained by investigating the filter's nonlinear operating points. For this, we propose mostly heuristic models for the CMOS inverters and the OTAs. Instead of modeling the input-output characteristic of the CMOS inverter, we model and combine the two internal MOSFETs it comprises. A detailed derivation of the CMOS inverter model used in this study can be found in our previous work [16]. We use the NMOS model in the form of

$$i_D = \begin{cases} 0 & \text{if } v_{GS} \leq v_T(v_{GS}) \\ i_{D,lin} & \text{if } v_{DS} \leq v_{GS} - v_T(v_{GS}) \wedge v_{GS} > v_T(v_{GS}) \\ i_{D,sat} & \text{otherwise} \end{cases} \quad (33a)$$

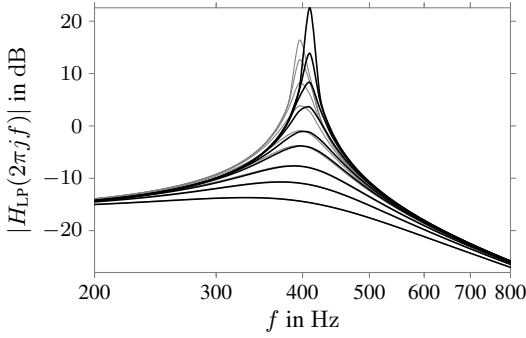
with

$$i_{D,lin} = \alpha(v_{GS}) \cdot (v_{GS} - v_T(v_{GS}) - \frac{v_{DS}}{2}) \cdot v_{DS} \cdot (1 + \lambda v_{DS}), \quad (33b)$$

$$i_{D,sat} = \frac{\alpha(v_{GS})}{2} \cdot (v_{GS} - v_T(v_{GS}))^2 \cdot (1 + \lambda v_{DS}) \quad (33c)$$



(a)



(b)

Figure 4: Magnitude transfer functions of lowpass  $H_{LP}$  (a) for various cutoff frequencies and  $\rho = 0.95$  and (b) for cutoff frequency  $\omega_c = 2\pi \cdot 400$  Hz and  $\rho \in \{0.1, 0.3, 0.5, 0.7, 0.8, 0.9, 0.95, 0.98, 1\}$ , zoomed in on the resonance frequency; linearized model in black, derived approximation as second-order SVF in gray

and

$$\alpha(v_{GS}) = c_{\alpha,2}v_{GS}^2 + c_{\alpha,1}v_{GS} + c_{\alpha,0} \quad (34a)$$

$$v_T(v_{GS}) = c_{v_T,2}v_{GS}^2 + c_{v_T,1}v_{GS} + c_{v_T,0}. \quad (34b)$$

This model can be parameterized by the linear regression coefficients  $c_{\alpha,i}$  and  $v_{T,i}$ , together with the channel length modulation coefficient  $\lambda$ . Note that the regression functions for the parameters  $\alpha$  and  $v_T$  can be also modified to higher-order polynomials depending on the specific device. The corresponding PMOS model can be derived similar to the NMOS model. The parameter optimization was performed using the differentiable white-box modeling approach presented in [17]. This process involves implementing the proposed NMOS and PMOS models inside a framework that allows automatic differentiation of computational graphs, such as Pytorch, and training its parameters to minimise a cost function based on measurement data from a real version of the system (the CD4069 CMOS inverters, in this case). The optimized coefficients for both MOSFETs of the CMOS inverter can be found in Table 2. Figure 5 shows the model output using the optimized parameters compared to the measurement data of the CD4069 inverter powered by +12 V.

Moving on to the OTAs, Fig. 6 shows the measured nonlinear current-voltage relationship of the CA3080 OTA. This saturating

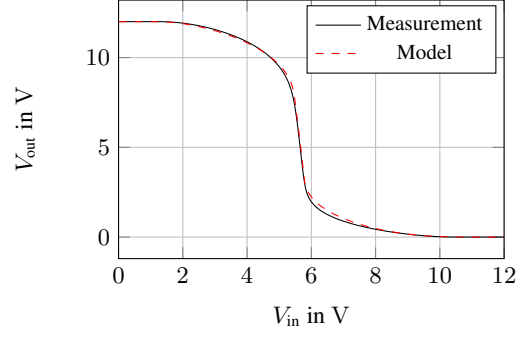


Figure 5: CMOS Inverter CD4069 Channel A

Parameter	Value
$c_{\alpha,0,n}$	0.0022
$c_{\alpha,1,n}$	$-1.0471 \cdot 10^{-4}$
$c_{\alpha,2,n}$	$3.1252 \cdot 10^{-6}$
$c_{v_T,0,n}$	0.8655
$c_{v_T,1,n}$	0.2212
$c_{v_T,1,n}$	0.0149
$\lambda_n$	$1 \cdot 10^{-3}$
$c_{\alpha,0,p}$	$-4.9942 \cdot 10^{-4}$
$c_{\alpha,1,p}$	$-5.1393 \cdot 10^{-4}$
$c_{\alpha,2,p}$	$-6.7622 \cdot 10^{-5}$
$c_{\alpha,3,p}$	$-2.7258 \cdot 10^{-6}$
$c_{v_T,0,p}$	0.6239
$c_{v_T,1,p}$	-0.1941
$c_{v_T,2,p}$	0.0135
$\lambda_p$	0.06

Table 2: Optimized MOSFET Parameters

behavior is typically modeled using a hyperbolic tangent as

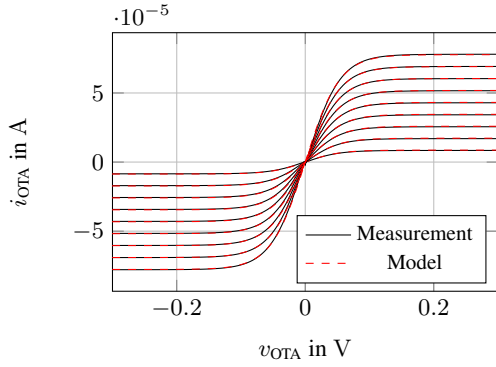
$$i_{OTA} = \alpha \cdot i_{bias} \tanh\left(\beta \frac{v_{OTA}}{2V_{TH}}\right), \quad (35)$$

where  $v_{OTA} = v_+ - v_-$  [13, 14]. The scaling parameters  $\alpha$  and  $\beta$  have been added in order to match the measured behavior. We again apply the same optimization scheme as for the CMOS inverters and obtain the optimum scaling parameters for ICs 2 and 4, which are listed in Table 3. Comparing the optimized model output to the measurement data from Fig. 6, it can be observed that the model is able to recreate the behavior of the OTA accurately.

Although this model is able to reproduce the nonlinear behavior of the OTA with respect to the differential input voltage  $v_{OTA}$ , it is missing an essential characteristic, which arises if a load in the form of a voltage source is connected to the OTA's output. Measurements for this configuration can be seen in Fig. 7. This figure shows the response of the output current  $i_{OTA}$  to a sweep of output voltage  $v_{out}$  for a set of different input voltages  $v_{OTA}$  and a

Parameter	Value
$\alpha$	0.8635
$\beta$	0.9408

Table 3: Optimized OTA Scaling Parameters


 Figure 6: OTA Output Current vs. Input Voltage,  $i_{bias} = 10\mu A$  to  $90\mu A$ 

fixed amplifier bias current  $i_{bias}$ . From (35) it can be implied that the output current should be independent from the output voltage; however, the measurements show a leap to different output currents at the supply rails of the OTA. We will see that modeling this non-ideal behavior at the amplifier's rails is crucial for recreating certain sounds of the Wasp filter. As a first step we create a relation between the plateau level at the rails and the input voltage  $v_{OTA}$  as well as the amplifier bias current  $i_{bias}$ . From the measurements, it can be observed that this relation can be modeled by a surface of the form

$$L(v_{OTA}, i_{bias}) = p_{L1} + p_{L2} \cdot i_{bias} + p_{L3} \cdot v_{OTA} + p_{L4} \cdot i_{bias}^2 + p_{L5} \cdot i_{bias} \cdot v_{OTA} \quad (36)$$

for the low supply rail and by

$$H(v_{OTA}, i_{bias}) = p_{H1} + p_{H2} \cdot i_{bias} + p_{H3} \cdot v_{OTA} + p_{H4} \cdot i_{bias}^2 + p_{H5} \cdot i_{bias} \cdot v_{OTA} \quad (37)$$

for the high supply rail. The transition between the output current level at the rails and the normal operation point can be modeled by a hyperbolic tangent as

$$f_H = \frac{H - f_M}{2} [\tanh(\gamma_H (v_{out} - \Delta v_H)) + 1] \quad (38)$$

and

$$f_L = -\frac{L - f_M}{2} [\tanh(\gamma_L (v_{out} - \Delta v_L)) - 1] \quad (39)$$

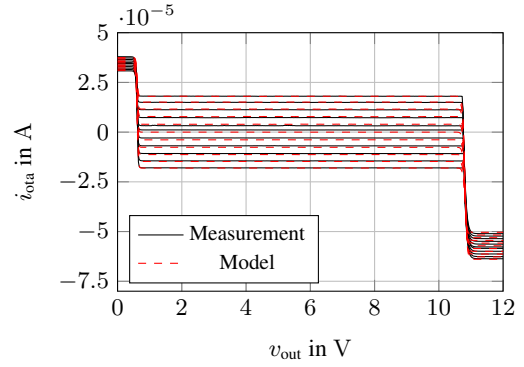
with  $f_M$  being the same equation as (35) i.e.

$$f_M = \alpha \cdot i_{bias} \tanh\left(\beta \frac{v_{OTA}}{2V_{TH}}\right). \quad (40)$$

We can now obtain a final equation for the output current by adding up all three functions

$$i_{OTA} = f_M + f_L + f_H. \quad (41)$$

Since the functions  $f_H$  and  $f_L$  will only affect the output current for output voltages near the rails, the characteristic behavior defined in (35) will remain unaffected. Applying yet again the same optimization scheme we find the optimum parameters for the extended OTA model, which are listed in Table 4. The corresponding model


 Figure 7: OTA Output Current vs. Output Voltage,  $i_{bias} = 50\mu A$ ,  $v_{ota}$  ranging from  $-20$  to  $20$  mA

output can be seen in Fig. 7. This leaves the diodes as the remaining nonlinear circuit components. The current through a diode can be modeled using Shockley's law as

$$i_d = I_s \left( e^{\frac{V_d}{\eta V_{TH}}} - 1 \right), \quad (42)$$

where  $I_s$  is the reverse saturation current and  $\eta$  is the ideality factor of the diode, which were optimized to 2.52 nA and 1.752 (dimensionless).

#### 4. SIMULATION RESULTS

In this section we will show simulation results for some key settings of the Wasp filter, especially focusing on its nonlinear nature and the need for an extended OTA model. All simulations were performed using the ACME framework [18] based on the white-box state-space approach from [19].

We start by demonstrating the effect of the resonance potentiometer. Therefore we use an exponential sinesweep signal of the form

$$u(n) = \sin\left(\frac{\Omega_1(L-1)}{\log\frac{\Omega_2}{\Omega_1}} \left(e^{\frac{n}{L-1} \log\frac{\Omega_2}{\Omega_1}} - 1\right)\right), \quad (43)$$

Parameter	Value
$p_{L1}$	$1 \cdot 10^{-9}$
$p_{L2}$	0.67938
$p_{L3}$	$1.27987 \cdot 10^{-7}$
$p_{L4}$	101.18857
$p_{L5}$	2.59819
$p_{H1}$	$91.7 \cdot 10^{-9}$
$p_{H2}$	-1.13642
$p_{H3}$	$-72 \cdot 10^{-9}$
$p_{H4}$	-170.11701
$p_{H5}$	-5.4144
$\gamma_L$	30.14
$\gamma_H$	16.0255
$\Delta v_H$	10.8105
$\Delta v_L$	0.6093

Table 4: Optimized OTA Rail Parameters

where  $L$  is the signal length and  $\Omega_1, \Omega_2$  are start and end normalized angular frequencies respectively. This will construct the first half of the input signal and the second half is the same sinesweep but starting at high and going back to low frequencies.

Figures 8 and 9 show the bandpass output for different resonance values of the Wasp filter. These plots also show the difference between the simple OTA model, which neglects the influence of the output voltage, and the extended model from (41). Taking a first a look at the measurements, the bandpass behavior of the filter can be spotted easily. The filter suppresses most of the frequency components except for a small band around the cut-off frequency. It can also be observed, that a high resonance value emphasizes the nonlinear nature of the filter, since the second half of the output signal is no longer symmetrical w.r.t. to the first half. In comparison, low resonance values result into a broader passband and a symmetrical behavior. This observation makes sense, since increasing the resonance value introduces more nonlinear feedback through the diodes D1, D2, as well as resistor  $R_4$ .

When comparing both OTA models, it can be observed that for small resonance values there is not much difference between the two results. For higher values however, the operation point at the output of the OTAs is shifting to values near the supply range. In this case the simple model is not able to follow the measurements at all, resulting into a shift of the cut-off frequency and a clipped output signal. In comparison, the model from (41) matches the envelope of the measured waveform accurately.

Even though these waveforms give us a first indication of the dynamic consequences of the different OTA models on the output signal, these results serve merely as a snapshot at a specific setting. To get a better understanding of the nonlinear dynamics, we can analyze the state-space data for the most dynamical states of the Wasp filter. As two states of interest we choose the voltages across capacitors  $C_3$  and  $C_4$ , which comprise the SVF integrators. Figures 10 and 11 show a random subset of the state-space data for the same input signal as in Figs. 8 and 9. As expected, both OTA models show a similar state-trajectory for a resonance value of 20%. The different behavior of the two models for high resonance values can be seen nicely in Fig. 11. Using the rail OTA model results into a state clipping near the OTA's supply voltage, whereas this behavior is completely missing when using the simple OTA model. Since the simple OTA model is not bounded by the output voltage  $v_{out}$ , the voltage over the capacitors can increase without any limitation, resulting into a clipped signal at the resonance frequency.

## 5. CONCLUSIONS

In this work we provided a virtual analog model for the Wasp VCF. We introduced extended models for OTA and CMOS inverters, which allowed a faithful digital representation of the filter. Especially the detailed modeling of the OTAs were a key feature to enable such a simulation. Although the results seem to be very positive, the proposed models need to be handled with care. Due to the fact that the models are based almost purely on measurement data, it is advised to use them only with input values in the range of the corresponding measurements. In this operation region, the results will be very precise if backed up by suitable measurements. To provide the most accurate model output it is also recommended to measure all circuit components prior to assembly if possible.

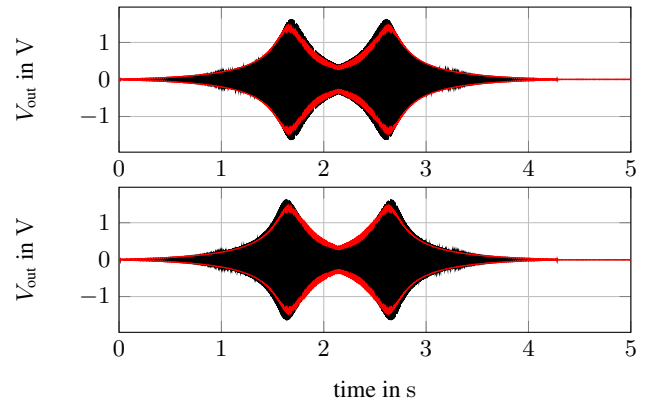


Figure 8: Output to Sinesweep Input, Resonance: 20%, Bias:  $7.42\mu\text{A}$ , Top: Simple OTA Model, Bottom: Rail OTA Model, Red: Envelope of Measurement

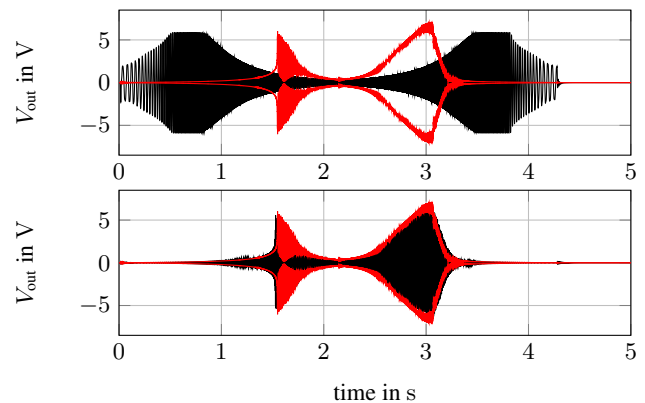


Figure 9: Output to Sinesweep Input, Resonance: 100%, Bias:  $7.42\mu\text{A}$ , Top: Simple OTA Model, Bottom: Rail OTA Model, Red: Envelope of Measurement

## 6. ACKNOWLEDGEMENTS

We would like to thank Dieter Döpfer of Doepfer Musikelektronik GmbH for the fruitful discussions on the design of the Wasp filter.

## 7. REFERENCES

- [1] P. Wiffen and M. Vail, "The Euro-Synth Industry," in *Vintage Synthesizers*, M. Vail, Ed., pp. 55–57. Miller Freeman Books, San Francisco, CA, USA, 2000.
- [2] C. Carter, "EDP Wasp," Available at <https://www.soundonsound.com/reviews/edp-wasp>, accessed April 09, 2022.
- [3] National Semiconductor Corporation, *CMOS Linear Applications*, Application Note 88. July 1973.
- [4] Doepfer Musikelektronik GmbH, "A-124 Wasp Filter," Available at <https://doepfer.de/a124.htm>, accessed April 11, 2022.
- [5] T. Stinchcombe, "EDP Gnat Synthesizer Schematics," Available at <https://www.timstinchcombe.co.uk/index.php?pge=gnat>, accessed April 12, 2022.
- [6] Novation Digital Music Systems Ltd., "Chris Huggett: Tributes from friends, colleagues and peers," Available at <https://novationmusic.com/en/news/chris-huggett-tributes>, accessed April 14, 2022.

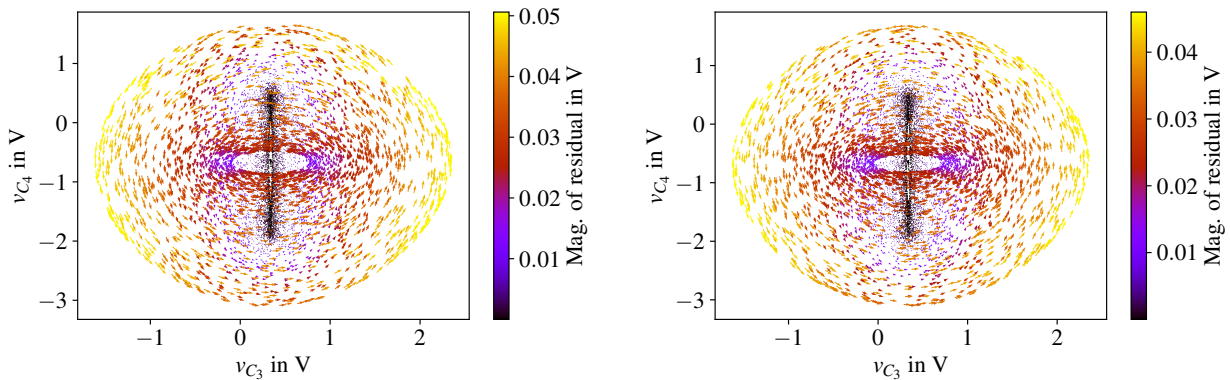


Figure 10: Subset of the state-space data for resonance=20% - left:simple OTA model, right: rail OTA model - colorbar: absolute value of the difference between two time-adjacent states

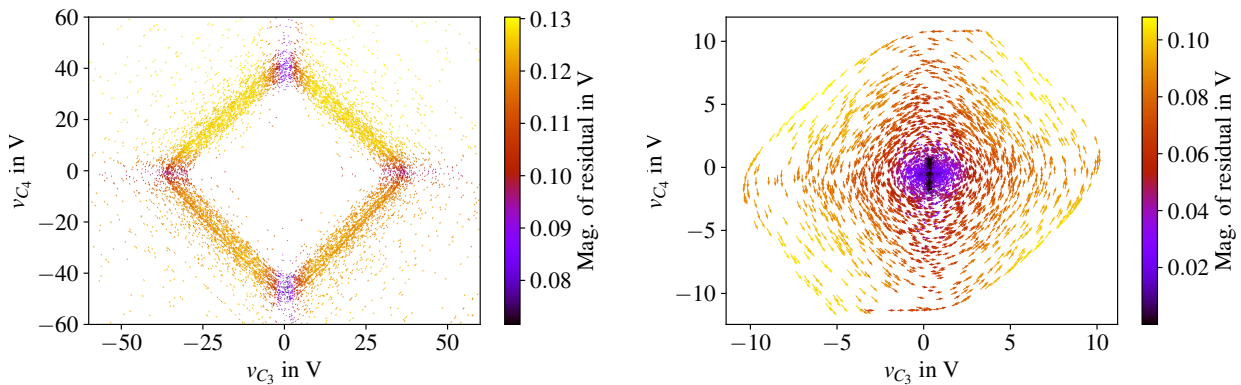


Figure 11: Subset of the state-space data for resonance=100% - left:simple OTA model, right: rail OTA model - colorbar: absolute value of the difference between two time-adjacent states

- [7] A. Huovilainen, “Non-linear digital implementation of the Moog ladder filter,” in *Proc. 7th Int. Conf. Digital Audio Effects (DAFx-04)*, Naples, Italy, Oct. 2004, pp. 61–64.
- [8] F. Fontana and M. Civolani, “Modeling of the EMS VCS3 voltage-controlled filter as a nonlinear filter network,” *IEEE Trans. Audio, Speech, Language Process.*, vol. 18, no. 4, pp. 760–772, Apr. 2010.
- [9] J. Parker, F. Esqueda, and A. Bergner, “Modelling of nonlinear state-space systems using a deep neural network,” in *Proc. 22nd Int. Conf. on Digital Audio Effects (DAFx-19)*, Birmingham, UK, 2019.
- [10] M. Rest, J. Parker, and K. J. Werner, “WDF modeling of a Korg MS-50 based non-linear diode bridge VCF,” in *Proc. 20th Int. Conf. Digital Audio Effects (DAFx-17)*, Edinburgh, UK, Sept. 2017, pp. 145–151.
- [11] W. J. Kerwin, L. P. Huelsman, and R. W. Newcomb, “State-variable synthesis for insensitive integrated circuit transfer functions,” *IEEE Journal of Solid-State Circuits*, vol. 2, no. 3, pp. 87–92, 1967.
- [12] B. Razavi, *Fundamentals of Microelectronics*, Wiley, Hoboken, NJ, 1st edition, 2008.
- [13] A. Huovilainen, “Enhanced digital models for analog modulation effects,” in *Proc. 8th Int. Conf. Digital Audio Effects (DAFx-05)*, Madrid, Spain, Sept. 2005, pp. 155–160.
- [14] Ó. Bogason and K. J. Werner, “Modeling circuits with operational transconductance amplifiers using wave digital filters,” in *Proc. 20th Int. Conf. Digital Audio Effects (DAFx-17)*, Edinburgh, UK, Sept. 2017, pp. 130–137.
- [15] D. Döpfer, Doepfer Musikelektronik GmbH, “Personal communication,” May 2022.
- [16] L. Köper and M. Holters, “Taming the Red Llama—modeling a CMOS-based overdrive circuit,” in *Proc. 23th Int. Conf. Digital Audio Effects (DAFx-2020)*, Vienna, Austria, Sept. 2020.
- [17] F. Esqueda, B. Kuznetsov, and J. D. Parker, “Differentiable white-box virtual analog modeling,” in *Proc. 24th Int. Conf. Digital Audio Effects (DAFx-20in21)*, Vienna, Austria, Sept. 2021.
- [18] M. Holters, “Analog Circuit Modeling and Emulation for Julia (v0.9.5),” Available at <https://github.com/HSU-ANT/ACME.jl>, accessed April 12, 2022.
- [19] M. Holters and U. Zölzer, “A generalized method for the derivation of non-linear state-space models from circuit schematics,” in *Proc. 23rd European Signal Process. Conf. (EUSIPCO)*, Nice, France, 2015, pp. 1078–1082.